

## **Supporting Information**

### **Unraveling Polymorphic Pyrrhotite Electrochemical Oxidation by Underlying Electronic Structures**

Chao Qi, Mohammad Khalkhali, James Grundy, Jing Liu, Jonathan Malainey, Qingxia Liu\*

*Department of Chemical and Materials Engineering, University of  
Alberta, Edmonton, Canada T6G 1H9*

\* Corresponding author: Dr. Qingxia Liu

Emails: [qingxia2@ualberta.ca](mailto:qingxia2@ualberta.ca)

Tel: +1 780 492-1119

## S1. DFT Simulation

There are major computational challenges when it comes to using DFT simulations to study pyrrhotite. First, there is great uncertainty regarding the crystal structure of defective FeS systems, particularly in the case of 5C-hexagonal pyrrhotite. The second major challenge is the size of the unit cells. Again, the 5C-hexagonal pyrrhotite is the major challenge as its unit cell is very big in the scale of DFT simulations. This means that pyrrhotite structures studied here contain many electrons which demand a considerable computational cost. The third challenge is that FeS compounds exhibit strong electron correlation due to the presence of iron. This correlation makes conventional DFT method inaccurate for these components and necessitates a computational method that can reasonably capture the effects of strong electron correlation. This method should also be computationally feasible for large periodic systems such as pyrrhotite. The DFT simulation parameters should be carefully chosen so we can perform the time-consuming DFT simulation with high certainty and minimal need for repeating.

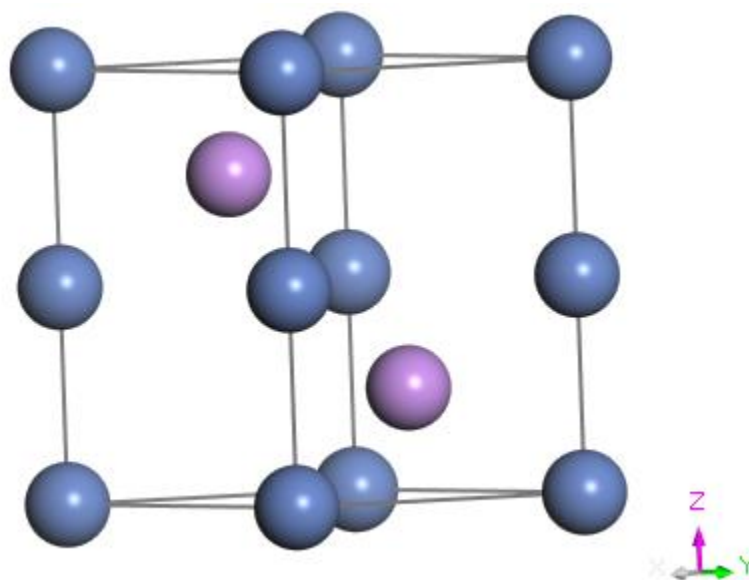


**Figure S1.** Schematic diagram of nickeline (NiAs) unit cell.

### S1.1 Geometry Optimization

The optimum value of  $U$  in the DFT+ $U$  method was determined by comparing the lowest energy structures with the experimentally measured unit cell. For this purpose, a series of geometry optimization simulations were performed for both 4C-monoclinic and 5C-hexagonal pyrrhotite using different  $U$  values. The value of  $U=1.8$  eV gave the best agreement between the calculated and experimentally measured unit cell volumes (**Fig. S2**).

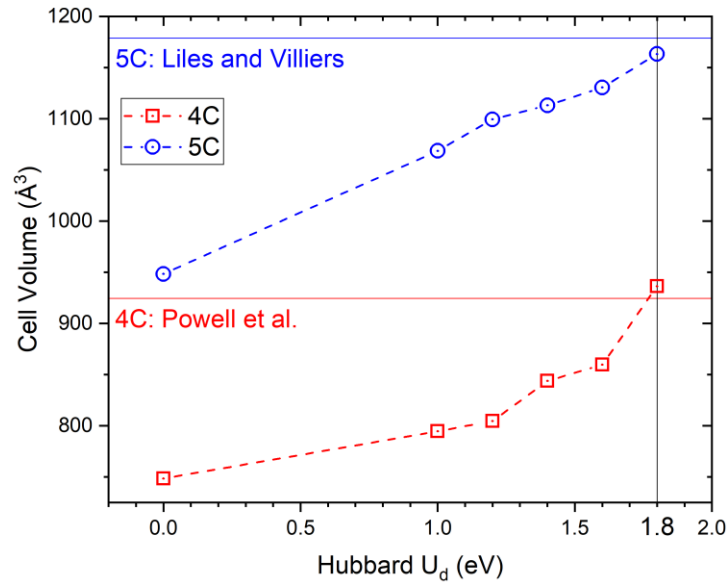


**Figure S2.** The relationship between  $U$  term in DFT+ $U$  calculations and cell volumes of 4C-monoclinic and 5C-hexagonal pyrrhotite. The horizontal straight lines show the corresponding experimental values (4C<sup>1</sup> and 5C<sup>2</sup>)

**Table S1.** The optimized crystal structures of 4C-monoclinic and 5C-hexagonal pyrrhotite calculated using  $U=1.8$  eV.

|              |                   | a (Å) | b (Å) | c (Å) | $\alpha$ (°) | $\beta$ (°) | $\gamma$ (°) | V (Å <sup>3</sup> ) |
|--------------|-------------------|-------|-------|-------|--------------|-------------|--------------|---------------------|
| 4C<br>(C2/c) | Calc.             | 11.87 | 6.92  | 12.92 | 90           | 118.02      | 90           | 936.40              |
|              | Exp. <sup>1</sup> | 11.87 | 6.85  | 12.90 | 90           | 118.075     | 90           | 924.58              |
| 5C           | Calc.*            | 6.89  | 28.55 | 6.83  | 89.55        | 119.98      | 89.91        | 1163.37             |
|              | Exp. <sup>2</sup> | 6.89  | 28.63 | 6.89  | 90           | 120         | 90           | 1178.27             |

\* To be able to model the 5C pyrrhotite with the spin configurations mentioned, the crystal should be modeled in P1 symmetry.

As mentioned in the simulation details of the paper, the  $U = 1.8$  eV was used to obtain the optimized unit cell structures of 4C-monoclinic and 5C-hexagonal pyrrhotite. The ferrimagnetic (4C) and anti-ferromagnetic (5C) spin configurations were assigned according to the atomic magnetic moment structure proposed by Wang and Salveson<sup>3</sup>. The monoclinic unit cell with C2/c symmetry<sup>1</sup> is well compatible with the ferrimagnetic structure of 4C-monoclinic pyrrhotite. However, we were not able to represent the anti-ferromagnetic structure of 5C-hexagonal pyrrhotite in any of the proposed symmetries. Thus, 5C-hexagonal unit cell was modeled in the P1 symmetry. The total magnetic moment of the 4C-monoclinic pyrrhotite optimized unit cell was  $3.92 \mu_B$  which is in a good agreement with the experimentally measured value of  $3.16 \mu_B$ <sup>1</sup>. **Table S1** shows the dimensions of the optimized unit cells.

### **S1.2 Electronic Structure**

**Fig. S3a** and **S3b** show the band structure for 4C-monoclinic and 5C-hexagonal pyrrhotite. Note that the band structure of the 5C-hexagonal pyrrhotite is denser due to more atoms in its unit cell.

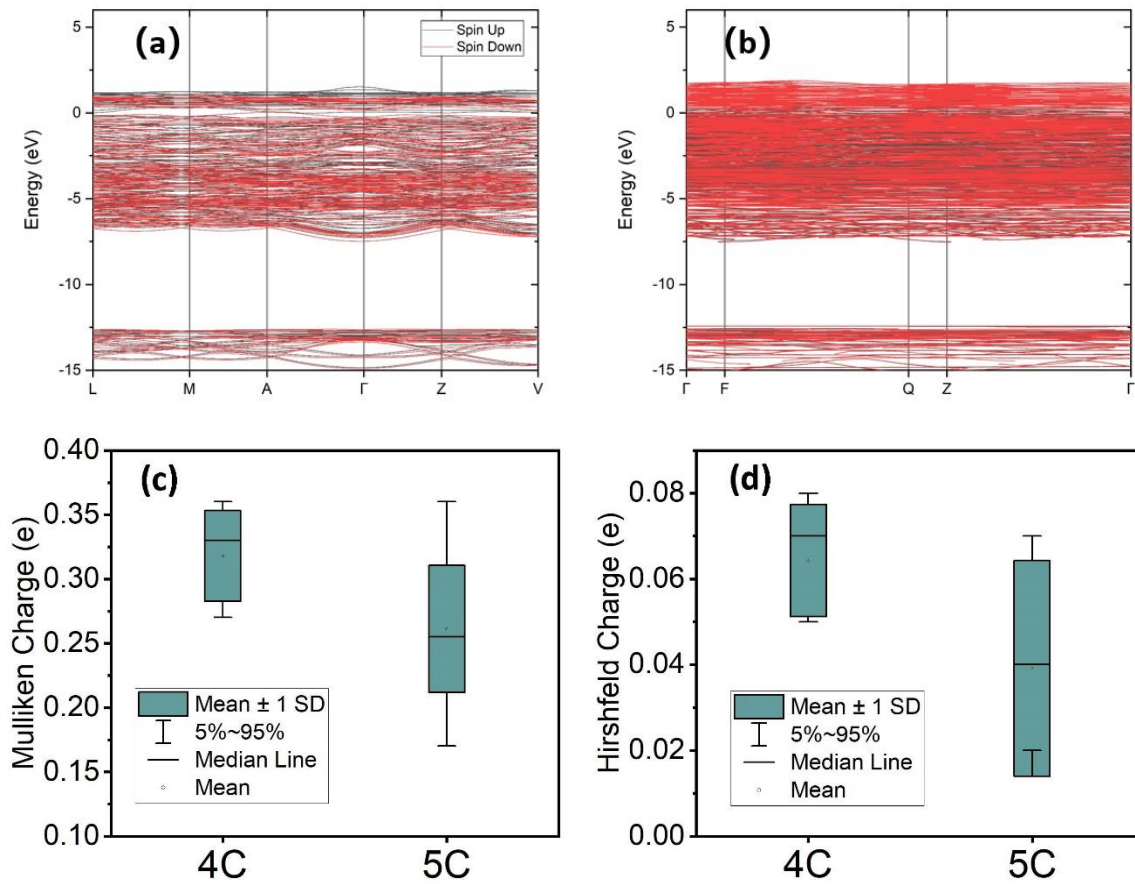


**Figure S3.** Band structure of 4C-monoclinic pyrrhotite (a) and 5C-hexagonal pyrrhotite (b); Average partial charges of iron atoms in 4C-monoclinic and 5C-hexagonal pyrrhotite calculated using Mulliken (c) and Hirshfeld (d) population analyses (Error bars represent the standard deviation)

For metallic components, its atomic chemical activity is also related to the amount of the available states near the Fermi level. To further analyze the electronic structure difference, we performed population analyses to calculate partial atomic charges. As CASTEP applies the plane-wave pseudopotential method, electrons localizations in the system are calculated via projecting the PW states onto a localized basis as explained by Sanchez-Portal et al.<sup>4</sup>. As **Fig. S3c** and **S3d** show, both Hirshfeld and Mulliken population analyses confirmed that iron atoms are more positively charged in the 4C pyrrhotite.

### S1.3 Band Center

The occupied bulk S  $3p$  band center and bulk Fe  $3d$  band center (**Fig. 4c**) were calculated with the formula (S1) <sup>5</sup>:

$$\text{band center} = \frac{\int E \cdot f(E) dE}{\int f(E) dE} \quad (\text{S1})$$

Here,  $E$  refers to the electron energy, and  $f(E)$  refers to their PDOS value.

### S1.4 Bond Strength

The average Fe-S bond length in two pyrrhotite structures was calculated and shown in **Fig. S4**. **Fig. S4** shows that the average Fe-S bond length is slightly smaller in 5C-hexagonal pyrrhotite. Although this difference is not considerable, it confirms the Fe-S bonding is stronger in 5C-hexagonal pyrrhotite than that in 4C-monoclinic pyrrhotite, consistent with the slightly higher  $\text{Fe}_2\text{S}^-/\text{FeS}^-$  intensity in hexagonal pyrrhotite deep layers (layers deeper than the III layer) than that in monoclinic pyrrhotite (see inset, **Fig. 3d**).

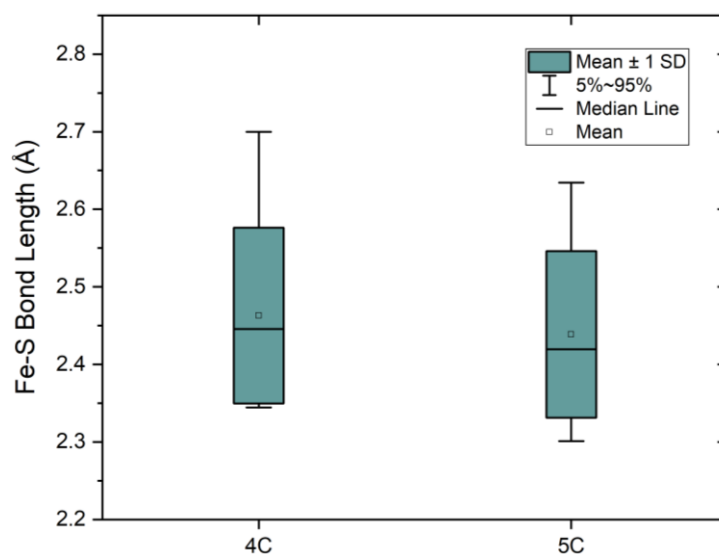


**Figure S4.** Average Fe-S bond length in optimized unit cells of 4C-monoclinic and 5C-hexagonal pyrrhotite (Error bars represent the standard deviation)

## S2. XPS Analysis Details

The S  $2p_{3/2}$  and S  $2p_{1/2}$  peaks are assigned to have the same full width at half maximum (FWHM) with an intensity ratio around 1.96:1 for the  $2p_{3/2}$ : $2p_{1/2}$  peaks <sup>6</sup>. The spin-orbit-split doublet S  $2p_{3/2}$  and S  $2p_{1/2}$  peak energies are split by 1.19 eV <sup>7</sup>. Note that only binding energies of the S  $2p_{3/2}$  are listed in **Table 3** of the paper.

According to Legrand<sup>8-9</sup> and Pratt<sup>10</sup>, iron can be affected by multiplet splitting due to unpaired electrons in the valence band, especially in intermediate and high spin states <sup>11-13</sup>. The parameters used for multiplet splitting for Fe  $2p_{3/2}$  in this paper are listed in **Table S2** <sup>10, 14</sup>. For a clear demonstration, their narrow spectra fitting peaks are shown in **Fig. S5**.

**Table S2.** Binding energies, FWHM and area ratio of multiplets for individual components of Fe(II)-S, Fe(III)-S, and Fe(III)-O used for fitting Fe 2p<sub>3/2</sub> <sup>14</sup>

| Species   | Peak     | Binding Energy<br>(eV) | FWHM<br>(eV) | Area |
|-----------|----------|------------------------|--------------|------|
| Fe(II)-S  | Multi. 1 | 706.2                  | 1.0          | 1.00 |
|           | Multi. 2 | 707.2                  | 1.2          | 3.80 |
|           | Multi. 3 | 708.1                  | 1.0          | 1.32 |
|           | Multi. 4 | 713.0                  | 2.6          | 1.61 |
| Fe(III)-S | Multi. 1 | 709.0                  | 1.3          | 1.00 |
|           | Multi. 2 | 710.1                  | 1.3          | 0.66 |
|           | Multi. 3 | 711.1                  | 1.3          | 0.35 |
|           | Multi. 4 | 712.0                  | 1.3          | 0.15 |
| Fe(III)-O | Multi. 1 | 710.4                  | 1.6          | 1.00 |
|           | Multi. 2 | 711.4                  | 1.6          | 0.95 |
|           | Multi. 3 | 712.6                  | 1.6          | 0.59 |
|           | Multi. 4 | 713.9                  | 1.6          | 0.28 |



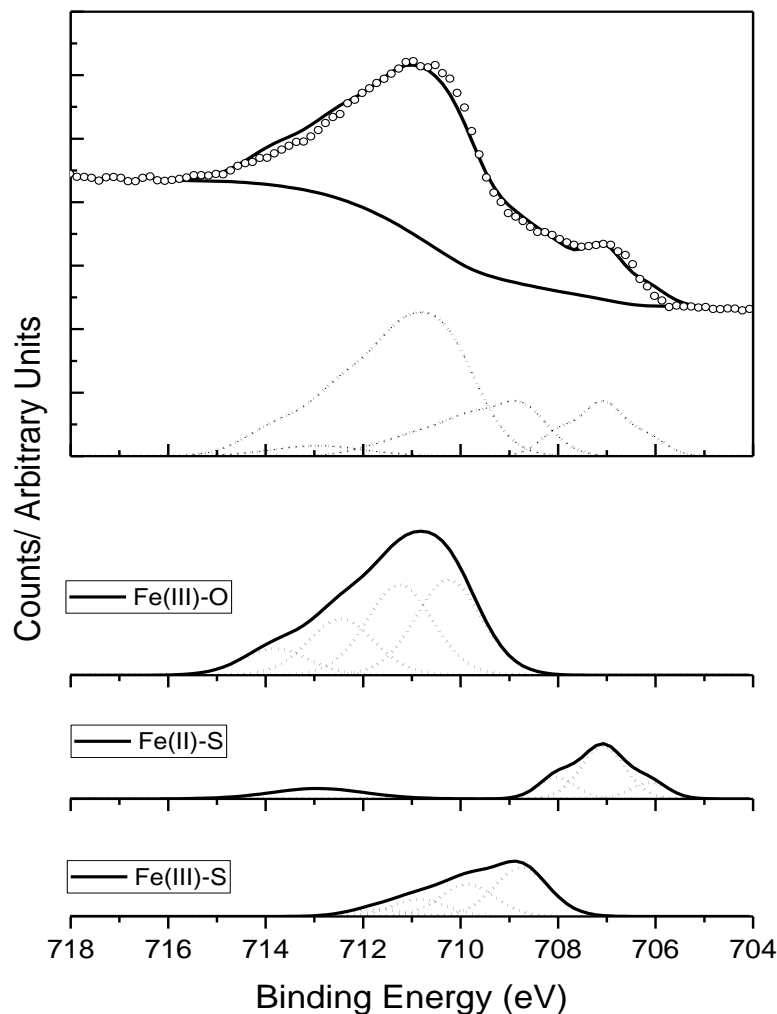


**Figure S5.** XPS Fe 2p<sub>3/2</sub> of oxidized monoclinic pyrrhotite. The top part is the fitting of the spectrum with only envelopes. The lower part is the detailed multiplet peaks for envelopes of different chemical species.

### S3. Chemical Reactions Summarized for CV studies

Chemical reactions happened at peak A<sub>1</sub> (**Fig. 1**) are summarized in **Table S3**.

**Table S3.** Summary of Electrochemical Reactions for the Anodic Peak A<sub>1</sub>

| Chemical Reaction Equations   | Potential  | Reference |
|---|--|-----------|
| $\text{Fe}_{(1-x)}\text{S} + 3y\text{OH}^- \rightarrow \text{Fe}_{(1-(x+y))}\text{S} + y\text{Fe}(\text{OH})_3 + 3ye^-$ | $E_h = E_h^0 - 0.059 \cdot \text{pH}$                                | 15-16     |
| $\text{FeS} + \text{H}_2\text{O} \rightarrow \text{Fe}(\text{OH})[\text{S}]^+ + \text{H}^+ + 2e^-$                      | $E_h = E_h^0 - 0.0295 \cdot \text{pH}$                               | 17        |
| $2\text{S}^{2-} \rightarrow \text{S}_2^{2-} + 2e^-$   | $E_h = E_h^0 + 0.059 \cdot \lg([\text{S}_2^{2-}]/[\text{S}^{2-}]^2)$ | 18        |

## S4. ToF-SIMS

### S4.1 Data Interpretation

ToF-SIMS data interpretation is complicated, and the model that could be used to fully interpret their data is still not known by the authors of this paper. As an important technique to learn about the defective layer properties, particularly the bond strength, ToF-SIMS principles used in the paper is presented here via Ignatova's work<sup>19-20</sup>. Ignatova did semi-quantitatively reproduce the ToF-SIMS depth profile data of ZrO<sub>2</sub>/SiO<sub>2</sub>/Si stacks with computer simulation, including the ZrO and SiO<sup>19-20</sup>. For the emission of ZrO and SiO, the O atom was picked up by a more reactive atom (Zr or Si)<sup>19-20</sup>. Since O atom needed to be picked up, a high molecular binding energy between O and Zr or Si is required. The simulation model proposed by Ignatova was presented as formula (S2)<sup>19-20</sup>.

$$Y_i^{mol} = g_i \cdot c_o \cdot Y_i^*(U_i^{mol}) \quad (S2)$$

Here,  $Y_i^{mol}$  refers to the molecular yield,  $c_o$  refers to the oxygen surface concentration,  $g_i$  indicates a probability factor, and  $Y_i^*(U_i^{mol})$  means a modified sputter yield characterized by its surface binding energy  $U_i^{mol}$ <sup>19-20</sup>.

For our case, we take FeS<sup>-</sup> as the reactive atom (one major species) and the emission of the Fe<sub>2</sub>S<sup>-</sup> therefore need a strong Fe-S bond to pick another iron out. So, the faster dropping of Fe<sub>2</sub>S<sup>-</sup>/FeS<sup>-</sup> inside monoclinic pyrrhotite in layer III than that of hexagonal pyrrhotite seems to suggest a faster dropping Fe-S bond strength inside monoclinic pyrrhotite than that of hexagonal pyrrhotite.

### S4.2 Sputtering Rate Estimation

According to Baryshev et al.<sup>21</sup>, the relation of the ToF-SIMS sputtering rate on pyrrhotite and silicon can be described as formula (S3).

$$\left(\frac{SR_{Po}}{SR_{Si}}\right) = \frac{U_{o, Si}}{U_{o, Po}} \frac{n_{Si}}{n_{Po}} \frac{\alpha_{Po}}{\alpha_{Si}} \frac{\gamma_{Po}}{\gamma_{Si}} \quad (S3)$$

Here,  $SR$  is the sputtering rate;  $U_{o, Si}$  and  $U_{o, Po}$  means the surface binding energy of silicon and pyrrhotite;  $n$  (atoms/volume) refers to the atomic density of the material, which can be calculated based on formula (S4)<sup>21</sup>;  $\alpha$  and  $\gamma$  are functions of number-average atomic mass  $M_t$  (formula (S7)) and the projectile atomic mass  $M_p$  ( $\text{Cs}^+$  in our case), as shown in formula (S5) and (S6)<sup>21</sup> respectively.

$$n = \frac{\rho}{M_t} \quad (S4)$$

$$\alpha = 0.08 + 0.164 \left(\frac{M_t}{M_p}\right)^{0.4} + 0.0145 \left(\frac{M_t}{M_p}\right)^{1.29} \quad (S5)$$

$$\gamma = \frac{4M_t M_p}{(M_t + M_p)^2} \quad (S6)$$

Here,  $M_t$  can be calculated based on formula (S7)<sup>21</sup>.

$$M_t = \frac{\sum v_i M_i}{\sum v_i} \quad (S7)$$

Here,  $v_i$  refers to the number of atoms of element  $i$  in the material,  $M_i$  is the atomic mass of the element  $i$ .

The surface binding energy of silicon  $U_{o, Si}$  was estimated to be 4.67 eV/atom<sup>22</sup>. The cohesive energy of monoclinic and hexagonal pyrrhotite is calculated with our DFT modeling work and listed in **Table S4**. With their cohesive energy, their surface binding energy could be calculated with formula (S8)<sup>21</sup>.

$$U_{o, Po} = \frac{E_{coh, Po}}{\sum v_i} \quad (S8)$$

Parameters used in the calculation are listed in **Table S4**. According to formula (S9)<sup>21</sup>, the ratio of sputtering rate on pyrrhotite against on silicon is 1.26 for both hexagonal and monoclinic pyrrhotite. Based on the sputtering rate on silicon (1.3 Å/s), the sputtering rate

on pyrrhotite is about 1.6 Å/s. Based on this, the thickness of the oxide layer, the polysulphide layer (from 65s to 200s in **Fig. 3**), and the defective layer (from 200s to 1500s in **Fig. 3**) are about 10.4, 21.6, and 208.0 nm.

$$\left(\frac{SR_{Po}}{SR_{Si}}\right) = \frac{U_{o,Si}}{U_{o,Po}} \frac{n_{Si}}{n_{Po}} \frac{\alpha_{Po}}{\alpha_{Si}} \frac{\gamma_{Po}}{\gamma_{Si}} \approx 1.26 \quad (S9)$$

**Table S4.** Summary of Parameters and Values Used for Estimating the ToF-SIMS Sputtering Rate.

| Parameter                | Value                 | Units                 |
|--------------------------|-----------------------|-----------------------|
| $E_{coh,hex-Po}$         | 313.72                | eV/unit cell          |
| $E_{coh,mono-Po}$        | 123.45                | eV/unit cell          |
| $\rho_{Po}$              | $4.6^{23}$            | $g/cm^3$              |
| $\rho_{Si}$              | $2.33^{24}$           | $g/cm^3$              |
| $M_{t,hex-Po}$           | 43.33                 | a.m.u.                |
| $M_{t,mono-Po}$          | 43.16                 | a.m.u.                |
| $M_{t,Si}$               | 28.09                 | a.m.u.                |
| $M_p$                    | 132.91                | a.m.u.                |
| $\gamma_{(Hex-Po, Cs)}$  | 0.74                  | -                     |
| $\gamma_{(Mono-Po, Cs)}$ | 0.74                  | -                     |
| $\gamma_{(Si, Cs)}$      | 0.58                  | -                     |
| $\alpha_{(Hex-Po, Cs)}$  | 0.19                  | -                     |
| $\alpha_{(Mono-Po, Cs)}$ | 0.19                  | -                     |
| $\alpha_{(Si, Cs)}$      | 0.17                  | -                     |
| $n_{(Hex,Po)}$           | $6.39 \times 10^{22}$ | $cm^{-3}$             |
| $n_{(Mono,Po)}$          | $6.42 \times 10^{22}$ | $cm^{-3}$             |
| $n_{(Si)}$               | $5.00 \times 10^{22}$ | $cm^{-3}$             |
| $U_{o,mono-Po}$          | 4.12                  | eV atom <sup>-1</sup> |
| $U_{o,hex-Po}$           | 4.13                  | eV atom <sup>-1</sup> |
| $U_{o,Si}$               | $4.67^{22}$           | eV atom <sup>-1</sup> |

\*Note that the cohesive energy and the surface binding energy listed in this table are their absolute value.

Note that the unit cell of monoclinic pyrrhotite contains 14 iron atoms and 16 sulfur atoms, meanwhile the unit cell of hexagonal pyrrhotite contains 36 iron atoms and 40 sulfur atoms.

## S5. Pyrrhotite Electrode Purity

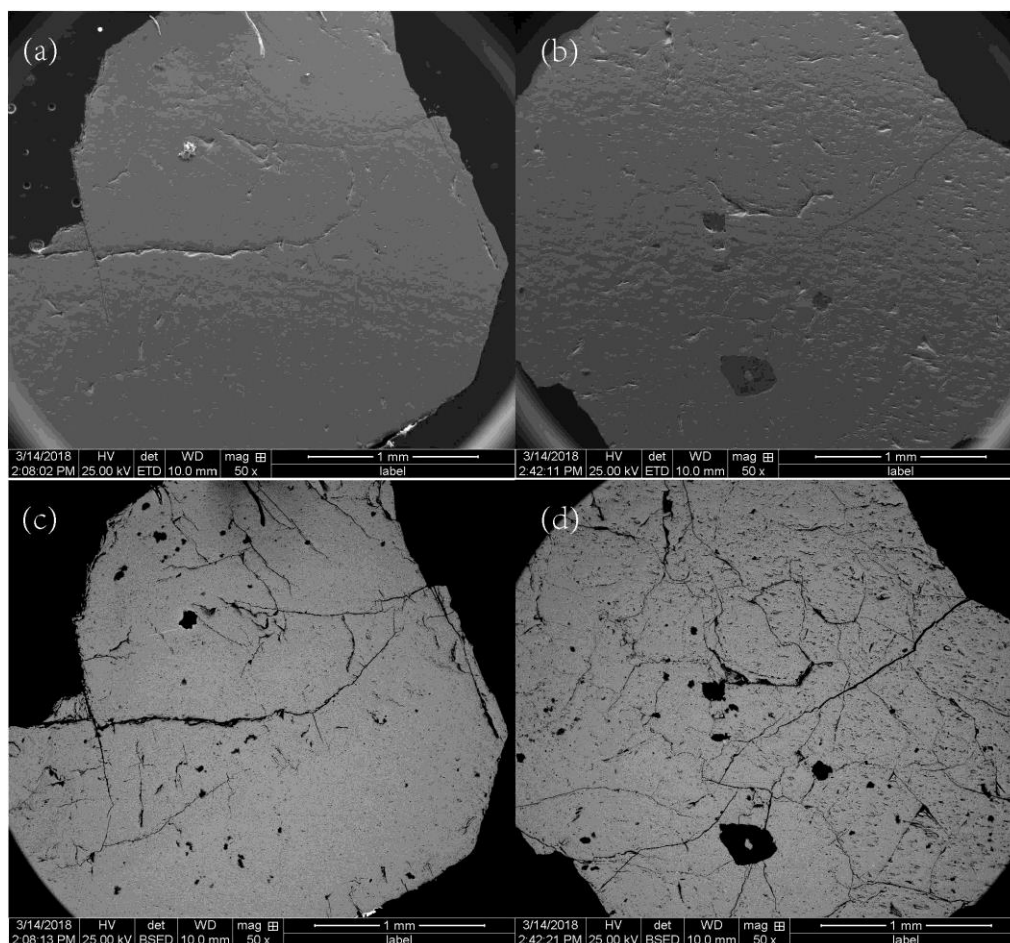


**Figure S6.** SEM and BSE images of the monoclinic (a-SEM, c-BSE) and hexagonal (b-SEM, d-BSE) pyrrhotite

In the SEM-based mineral liberation analysis, different minerals can be distinguished solely based on the backscattered electron (BSE) image grey level contrast. In our experiment, both SEM images and BSE images (**Fig. S6**) are listed to demonstrate their purity. As shown in **Fig. S6c** and **S6d**, slight amount of impurities do exist but the main part of both pyrrhotites BSE images is of same grey level, indicating that the overall purity of both pyrrhotites is good enough for our XPS and ToF-SIMS analysis. Note that most dark areas in **Fig. S6c** and **S6d** are a result of crevices. Their main composition was analyzed with the Energy-dispersive X-ray Spectroscopy (EDX). The EDX results showed

that main part of hexagonal pyrrhotite is composed of 61.81% Fe and 38.19% S; meanwhile, the monoclinic pyrrhotite is composed of 61.34% Fe and 38.66% S.

## Reference

1. Powell, A. V.; Vaquero, P.; Knight, K. S.; Chapon, L. C.; Sánchez, R. D., Structure and Magnetism in Synthetic Pyrrhotite  $\text{Fe}_7\text{S}_8$ : A Powder Neutron-Diffraction Study. *Physical Review B* **2004**, *70*, 014415.
2. Liles, D. C.; de Villiers, J. P., Redetermination of the Structure of 5C Pyrrhotite at Low Temperature and at Room Temperature. *American Mineralogist* **2012**, *97*, 257-261.
3. Wang, H.; Salveson, I., A Review on the Mineral Chemistry of the Non-Stoichiometric Iron Sulphide,  $\text{Fe}_{1-x}\text{S}$  ( $0 \leq x \leq 0.125$ ): Polymorphs, Phase Relations and Transitions, Electronic and Magnetic Structures. *Phase Transitions* **2005**, *78*, 547-567.
4. Sanchez-Portal, D.; Artacho, E.; Soler, J. M., Projection of Plane-Wave Calculations into Atomic Orbitals. *Solid State Communications* **1995**, *95*, 685-690.
5. Tao, H.; Liu, S.; Luo, J.-L.; Choi, P.; Liu, Q.; Xu, Z., Descriptor of Catalytic Activity of Metal Sulfides for Oxygen Reduction Reaction: A Potential Indicator for Mineral Flotation. *Journal of Materials Chemistry A* **2018**, *6*, 9650-9656.
6. Scofield, J. H., Hartree-Slater Subshell Photoionization Cross-Sections at 1254 and 1487 Ev. *Journal of Electron Spectroscopy and Related Phenomena* **1976**, *8*, 129-137.
7. Schaufuß, A. G.; Nesbitt, H. W.; Kartio, I.; Laajalehto, K.; Bancroft, G. M.; Szargan, R., Reactivity of Surface Chemical States on Fractured Pyrite. *Surface Science* **1998**, *411*, 321-328.
8. Legrand, D. L., Oxidation/Alteration of Pentlandite and Pyrrhotite Surfaces at pH 9.3: Part 1. Assignment of Xps Spectra and Chemical Trends. *American Mineralogist* **2005**, *90*, 1042-1054.
9. Legrand, D. L., Oxidation of Pentlandite and Pyrrhotite Surfaces at pH 9.3: Part 2. Effect of Xanthates and Dissolved Oxygen. *American Mineralogist* **2005**, *90*, 1055-1061.
10. Pratt, A.; Nesbitt, H., Generation of Acids from Mine Waste: Oxidative Leaching of Pyrrhotite in Dilute  $\text{H}_2\text{SO}_4$  Solutions at pH 3.0. *Geochimica et Cosmochimica Acta* **1994**, *58*, 5147-5159.
11. Mikhlin, Y.; Tomashevich, Y., Pristine and Reacted Surfaces of Pyrrhotite and Arsenopyrite as Studied by X-Ray Absorption near-Edge Structure Spectroscopy. *Physics and Chemistry of Minerals* **2005**, *32*, 19-27.
12. Biesinger, M. C.; Payne, B. P.; Grosvenor, A. P.; Lau, L. W.; Gerson, A. R.; Smart, R. S. C., Resolving Surface Chemical States in Xps Analysis of First Row Transition Metals, Oxides and Hydroxides: Cr, Mn, Fe, Co and Ni. *Applied Surface Science* **2011**, *257*, 2717-2730.
13. Moulder, J.; Stickle, W.; Sobol, P.; Bomben, K., Handbook of X-Ray Photoelectron Spectroscopy (Perkin-Elmer, Eden Prairie, Mn, 1992). *Google Scholar* **2002**, 128.
14. Qi, C.; Liu, J.; Malainey, J.; Kormos, L. J.; Coffin, J.; Deredin, C.; Liu, Q.; Fragomeni, D., The Role of Cu Ion Activation and Surface Oxidation for Polymorphic Pyrrhotite Flotation Performance in Strathcona Mill. *Miner Eng* **2019**, *134*, 87-96.
15. Buswell, A.; Nicol, M., Some Aspects of the Electrochemistry of the Flotation of Pyrrhotite. *Journal of applied electrochemistry* **2002**, *32*, 1321-1329.
16. Ekmekçi, Z.; Becker, M.; Tekes, E. B.; Bradshaw, D., The Relationship between the Electrochemical, Mineralogical and Flotation Characteristics of Pyrrhotite Samples from Different Ni Ores. *Journal of Electroanalytical Chemistry* **2010**, *647*, 133-143.
17. Hodgson, M.; Agar, G., Electrochemical Investigations into the Flotation Chemistry of Pentlandite and Pyrrhotite: Process Water and Xanthate Interactions. *Canadian Metallurgical Quarterly* **1989**, *28*, 189-198.
18. Mikhlin, Y., Reactivity of Pyrrhotite Surfaces: An Electrochemical Study. *Phys Chem Chem Phys* **2000**, *2*, 5672-5677.

19. Ignatova, V.; Conard, T.; Möller, W.; Vandervorst, W.; Gijbels, R., Depth Profiling of  $\text{ZrO}_2/\text{SiO}_2/\text{Si}$  Stacks—a ToF-Sims and Computer Simulation Study. *Applied surface science* **2004**, *231*, 603-608.
20. Ignatova, V.; Möller, W.; Conard, T.; Vandervorst, W.; Gijbels, R., Interpretation of ToF-SIMS Depth Profiles from Ultrashallow High-K Dielectric Stacks Assisted by Hybrid Collisional Computer Simulation. *Applied Physics A* **2005**, *81*, 71-77.
21. Baryshev, S. V.; Thimsen, E., Enthalpy of Formation for Cu–Zn–Sn–S (Czts) Calculated from Surface Binding Energies Experimentally Measured by Ion Sputtering. *Chemistry of Materials* **2015**, *27*, 2294-2298.
22. Borrajo-Pelaez, R.; Saiz, F.; Gamero-Castaño, M., The Effect of the Molecular Mass on the Sputtering of Si, SiC, Ge, and GaAs by Electrosprayed Nanodroplets at Impact Velocities up to 17 Km/S. *Aerosol Science and Technology* **2015**, *49*, 256-266.
23. Henkel, H., Standard Diagrams of Magnetic Properties and Density—a Tool for Understanding Magnetic Petrology. *Journal of Applied Geophysics* **1994**, *32*, 43-53.
24. Fujii, K.; Tanaka, M.; Nezu, Y.; Sakuma, A.; Leistner, A.; Giardini, W., Absolute Measurement of the Density of Silicon Crystals in Vacuo for a Determination of the Avogadro Constant. *IEEE transactions on instrumentation and measurement* **1995**, *44*, 542-545.